Environmental Fluid Mechanics (2020) 20:1637–1662
https://doi.org/10.1007/s10652-020-09758-2

ORIGINAL ARTICLE

Experiments on gravity currents propagating on unbounded uniform slopes

Albert Dai[1] · **Yu-Lin Huang**[1]

Received: 15 December 2019 / Accepted: 14 July 2020 / Published online: 29 July 2020

Abstract
Gravity currents propagating on 12°, 9°, 6°, 3° unbounded uniform slopes and on an unbounded horizontal boundary are reported. Results show that there are two stages of the deceleration phase. In the early stage of the deceleration phase, the front location history follows $(x_f + x_0)^2 = (K_I B)^{1/2}(t + t_I)$, where $(x_f + x_0)$ is the front location measured from the virtual origin, K_I an experimental constant, B the total buoyancy, t time and t_I the t-intercept. In the late stage of the deceleration phase for the gravity currents on 12°, 9°, 6° unbounded uniform slopes, the front location history follows $(x_f + x_0)^{8/3} = K_{VS} B^{2/3} V_0^{2/9} \nu^{-1/3}(t + t_{VS})$, where K_{VS} is an experimental constant, V_0 the initial volume of heavy fluid, ν the kinematic viscosity and t_{VS} the t-intercept. In the late stage of the deceleration phase for the gravity currents on a 3° unbounded uniform slope and on an unbounded horizontal boundary, the front location history follows $(x_f + x_0)^4 = K_{VM} B^{2/3} V_0^{2/3} \nu^{-1/3}(t + t_{VM})$, where K_{VM} is an experimental constant and t_{VM} the t-intercept. Two qualitatively different flow morphologies are identified in the late stage of the deceleration phase. For the gravity currents on 12°, 9°, 6° unbounded uniform slopes, an 'active' head separates from the body of the current. For the gravity currents on a 3° unbounded uniform slope and on an unbounded horizontal boundary, the gravity currents maintain an integrated shape throughout the motion. Results indicate two possible routes to the final stage of the gravity currents on unbounded uniform slopes.

Keywords Gravity currents · Deceleration phase · Unbounded uniform slope

1 Introduction

Gravity currents, which are flows driven by density differences, occur in many natural and man-made environments [46, 49]. The density differences may be attributed to a number of factors, including temperature differentials, dissolved materials and suspended sediments. The lock-exchange set-up has long served as a paradigm configuration for studying the evolution of gravity currents [1, 22–25, 34, 38, 45]. In the classic lock-exchange

✉ Albert Dai
hdai@ntu.edu.tw

[1] Department of Engineering Science and Ocean Engineering, National Taiwan University, Taipei, Taiwan

experiments, two fluids of different densities are separated by a removable gate in a long, horizontal channel and, after the gate is removed, the heavy fluid travels along the bottom boundary in the streamwise direction and the light ambient fluid travels along the top boundary in the opposite direction. Such gravity currents are also called the planar gravity currents as the flows are bounded by the channel walls and the structures of the gravity currents are statistically homogeneous in the spanwise direction.

Gravity currents may occur not only on a horizontal plane but also on a sloping boundary. In the literature, some studies investigated the planar gravity currents propagating on a favourable slope [3, 4, 8, 10–12, 29–31, 33, 37, 39, 40, 43, 47, 51] while some others investigated the planar gravity currents propagating on an adverse slope [20, 27, 28, 35, 36]. For the planar gravity currents propagating down a slope [3], it was observed that the gravity currents may go through an acceleration phase followed by a deceleration phase and developed the thermal theory to describe the two phases of motion. The deceleration phase of the planar gravity currents down a slope was further categorised into an early stage where the buoyancy force is in balance with the inertia force and a late stage where the buoyancy force is in balance with the viscous force [8, 10]. The front location history of the planar downslope gravity currents follows different power-relationships in the early deceleration phase and in the late deceleration phase.

Gravity currents may also propagate radially outward without being bounded in the spanwise direction by the channel walls [5, 14, 19, 26, 41, 42]. For the gravity currents propagating down an unbounded uniform slope, the gravity currents may propagate in both the streamwise and spanwise directions. This configuration is more similar to that of turbidity currents down a continental shelf and powder snow avalanches [16]. Using the shallow water model, it was predicted that the gravity currents on an unbounded uniform slope would take a self-similar cylindrical wedge shape [48, 50] . It was shown experimentally [44] and computationally [52] that such gravity currents take a shape which is similar to a triangular wedge or a boomerang.

Consistent with the planar gravity currents propagating down a slope, the gravity currents propagating on an unbounded uniform slope may also go through the acceleration phase followed by the deceleration phase. For the acceleration phase of propagation, using high-resolution direct numerical simulations, the gravity currents on an unbounded uniform slope for a range of slope angles between 5° and 20° were investigated in [52] and two consecutive acceleration phases were detected. It was reported that the first acceleration phase occurs when the heavy fluid initially advances in a diverging manner and the second acceleration phase occurs when the heavy fluid converges towards the centre of the gravity currents due to the presence of a slope. After the two consecutive acceleration phases, the gravity currents on an unbounded uniform slope move into the deceleration phase. For the deceleration phase of propagation, it was shown in [44] that the front location history was well described by the wedge integral model for the whole range of the deceleration phase. The wedge integral model, developed by [44], is essentially in the same spirit as [32] and the subsequent thermal theory adopted in [3, 6–10] for the gravity currents on an inclined boundary with bounded walls.

As explained above, while most previous investigations, including the ones published by the authors, were focused on the gravity currents confined in the spanwise direction by the channel walls, there was less attention focused on the gravity currents propagating on slopes without being bounded in the streamwise and spanwise directions. For the gravity currents confined in the spanwise direction, i.e. the planar gravity currents, the gravity currents can grow in the streamwise and wall-normal directions and are theoretically treated as two-dimensional. For the gravity currents propagating on slopes without being bounded

in the streamwise and spanwise directions, the gravity currents can grow in the streamwise, spanwise and wall-normal directions and should be theoretically treated as three-dimensional. In the literature, for the gravity currents on unbounded uniform slopes, only one deceleration phase was identified and the wedge integral model was found to appropriately describe the front location history in the deceleration phase. We aim at deepening the understanding of the gravity currents on unbounded uniform slopes by performing laboratory experiments and, as will be shown in the following sections, two stages of the deceleration phase can be identified and the wedge integral model is appropriate only for the early stage of the deceleration phase.

In this study, we investigated the gravity currents produced from a finite volume of heavy fluid propagating on different unbounded uniform slopes. The density difference between the heavy fluid and the ambient fluid is sufficiently small so that our experiments may be classified as Boussinesq. Our focus in this study is on the deceleration phase of propagation of the gravity currents. As will be shown in more detail, the asymptotic relationship for the front location history based on the wedge integral model applies only for the early stage of the deceleration phase. In the late stage of the deceleration phase, different flow morphologies and relationships for the front location history are identified and reported here for the first time. Specifically, using the laboratory experiments, we may qualitatively observe how the gravity currents propagate on an unbounded uniform slope and quantitatively measure the influence of the slope in the early stage and late stage of the deceleration phase. In Sect. 2, we summarize the theoretical relationships for the front location history in the early and late stage of the deceleration phase. The experimental setup and techniques are described in Sect. 3. Qualitative and quantitative results are presented in Sect. 4 and the conclusions are drawn in Sect. 5.

2 Theoretical background

The configuration of the problem is sketched in Fig. 1. Here we summarize the wedge integral model developed by [44] and follow the nomenclature therein for the reader's convenience. The density of heavy fluid in the lock is ρ_1 and the density of light ambient fluid is ρ_0. As an approximation in the model, it is assumed that the gravity currents maintain a self-similar wedge geometry [44, 48, 50]. The overall width and height of the self-similar wedge prescribed by [50] are $b = \pi l$ and $h = l\tan\theta$, respectively, where l represents the length of the wedge. The top area and front area of the wedge are given by $A_T = S_1 l^2$ and $A_F = S_2 l^2 \tan\theta$, respectively, and the wedge volume is $V = S_3 l^3 \tan\theta$, where S_1, S_2 and S_3 are the shape factors. For the cylindrical wedge shape given by [50], the shape factors take the values $S_1 = 3\pi/4$, $S_2 = 8/3$ and $S_3 = 5\pi/16$. It is worth noting that the wedge integral model is not restricted to the shape prescribed by the shallow water model of [50] but can be applied for other self-similar wedge shapes. When other self-similar wedge shapes are used, different values for the shape factors are adopted. As indicated by [44], for a self-similar wedge with a triangular top, the shape factors $S_1 = 1$, $S_2 = \sqrt{2}$ and $S_3 = 1/3$ should be in use.

The motion of the gravity currents is driven by the density difference between the heavy fluid contained within the wedge and the ambient fluid. We assume that the density difference is small, i.e. $(\rho_1 - \rho_0) \ll \rho_0$, such that the Boussinesq approximation applies. Therefore, following [44], the linear momentum equation takes the form

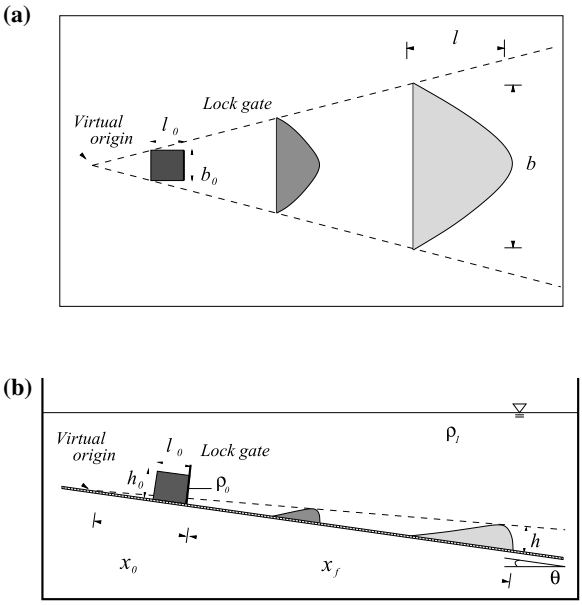

Fig. 1 Sketch of the experimental setup and the wedge integral model for the gravity currents produced from a finite volume of heavy fluid propagating on an unbounded uniform slope, which makes an angle θ with the horizontal plane. **a** top view and **b** side view of the tank. In **a**, the length and width of the wedge are designated by l and b, respectively. In **b**, the height of the wedge is designated by h. The heavy fluid initially contained in the lock has density ρ_1 while the ambient fluid has density ρ_0. The front location x_f is measured from the lock gate and the virtual origin is at a distance x_0 upslope of the lock gate. The lock has length $l_0 = 10$ cm, width $b_0 = 10$ cm and height $h_0 = 8$ cm in all experiments

$$\frac{d}{dt}\left[\left(1 + C_A\right)VU\right] = B\sin\theta - \left(C_T A_T + C_F A_F\right)U^2, \tag{1}$$

where C_A is the 'added mass' coefficient, which takes into account the ambient fluid carried along with the gravity currents, U the velocity of the centre of mass of the current wedge, $B = V_0 g(\rho_1 - \rho_0)/\rho_0$ the buoyancy which is conserved during the propagation of the gravity currents, C_T and C_F the bottom and form drag coefficients and t the time. The added mass coefficient cannot be calculated easily for the gravity current wedge, which deforms and entrains ambient fluid while propagating on a slope. However, it is reasonable to estimate the added mass coefficient based on those for similar typical shapes [3]. The values for a circular cylinder and a sphere are given as 1 and 0.5, respectively, by [2]. For a streamlined wedge of width b and length l, the added mass coefficient for the wedge is estimated as $C_A = 0.5$ in this study [21]. For turbulent flows in the experiments, the drag force is modeled as being proportional to velocity squared. In fact, it was showed in [44] that the influence of adding the drag force is negligible and it was also shown in [9] that the dominant retarding mechanism is the entrainment of ambient fluid and excluding the drag force term from the momentum equation does not alter the form of the asymptotic relationship for the front location history in the deceleration phase.

With the assumption of turbulent entrainment [15], the mass conservation takes the form

$$\frac{dV}{dt} = \alpha U A_E, \tag{2}$$

where α is the entrainment coefficient and $A_E = S_4 l^2 \tan\theta$ is the area over which the entrainment takes place, where S_4 is another shape factor. We could have separate terms for the entrainment over top and front areas, with different entrainment coefficients. However, it can be shown that for the self-similar wedge shape the two terms for the entrainment

are proportional and may be absorbed into one term [48]. A similar assumption of one entrainment coefficient was also applied in the model of [26] for simulating unconfined gravity currents. For the cylindrical wedge shape given by [50], $S_4 = \pi\sqrt{2}$ and for the triangular wedge shape, $S_4 = 2\sqrt{2}$ as chosen by [44] and followed here. From (2) and using $U = dx/dt$, we may derive

$$l = \frac{S_4\alpha}{3S_3}x, \tag{3}$$

where x is the distance measured from the 'virtual origin' to the centre of mass of the wedge. The 'virtual origin' is located x_0 upslope of the lock gate and can be identified by extrapolating the development of the width of the wedge in the upslope direction, as shown in Fig. 1. Upon substituting (3) into (1) and again using $U = dx/dt$, we may derive the solution for the momentum equation, i.e.

$$U^2 = U_\infty^2\left(\frac{x_0}{x}\right)^2 + \left(U_0^2 - U_\infty^2\right)\left(\frac{x_0}{x}\right)^\gamma, \tag{4}$$

where

$$U_\infty^2 = \frac{54BS_3^2\cos\theta}{x_0^2\alpha^3S_4^3(1+C_A)(\gamma-2)} \quad \text{and} \quad \gamma = 6\left(1 + \frac{C_TS_1 + C_FS_2\tan\theta}{\alpha S_4\tan\theta(1+C_A)}\right). \tag{5}$$

When the gravity currents start from rest, the model predicts that, after an initial acceleration phase, the centre of mass of the current wedge reaches a maximum velocity at the downstream location

$$\frac{x}{x_0} = \left(\frac{\gamma}{2}\right)^{1/(\gamma-2)}. \tag{6}$$

In the limit when the bottom and form drags are negligible, i.e. $C_T \to 0$ and $C_F \to 0$, the centre of mass velocity reaches its maximum at $x/x_0 \to 3^{1/4}$. After the initial acceleration phase, the centre of mass velocity of the wedge decreases with the distance measured from the virtual origin. When the gravity currents are sufficiently far into the deceleration phase, i.e. $x/x_0 \gg 1$, the centre of mass velocity of the wedge approaches the following asymptote

$$U = \frac{54^{1/2}B^{1/2}S_3\cos^{1/2}\theta}{\alpha^{3/2}S_4^{3/2}\sqrt{(1+C_A)}\sqrt{(\gamma-2)}}x^{-1}. \tag{7}$$

Since the front location is a more easily measurable quantity than the centre of mass of the wedge, we rewrite the solution (7) in terms of the front location, x_f, which is measured from the lock gate. Using the geometric relation for a triangular wedge $x_f + x_0 = x + l/2$, i.e. $x_f + x_0 = \left(1 + S_4\alpha/6S_3\right)x$, the front velocity in the deceleration phase approaches the following asymptote

$$U_f = \left(1 + \frac{\alpha S_4}{6S_3}\right)^2 \frac{54^{1/2}B^{1/2}S_3\cos^{1/2}\theta}{\alpha^{3/2}S_4^{3/2}\sqrt{(1+C_A)}\sqrt{(\gamma-2)}} \times (x_f + x_0)^{-1}, \tag{8}$$

Upon integration, (8) can be rewritten in the following form with an integration constant t_I

$$(x_f + x_0)^2 = \left(K_I B\right)^{1/2}(t + t_I), \tag{9}$$

where K_I follows the form

$$K_I = \left(1 + \frac{\alpha S_4}{6S_3}\right)^4 \frac{216 S_3^2 \cos\theta}{\alpha^3 S_4^3 (1 + C_A)(\gamma - 2)}, \tag{10}$$

which is independent of the buoyancy and is a function of the slope angle. From (9), it is clear that when the front location history is plotted in terms of $(x_f + x_0)^2$ versus t, the slope in the deceleration phase can be measured from the experimental data and should be $(K_I B)^{1/2}$. Therefore, the experimental constant K_I can be calculated based on the measured slope in the plot of $(x_f + x_0)^2$ versus t in the deceleration phase and the total buoyancy B. Once the experimental constant K_I is determined, we may calculate the entrainment coefficient α with the help of (10). While the 'virtual origin' is identified as explained above, we do not have control over the t-intercept t_I in (9). The t-intercept t_I is identified by finding the point where (9) crosses the t-axis. In our study, t_I does not have physical significance but we still include t_I for completeness as will be shown later in Table 2. We are particularly concerned about the slope in the plot of $(x_f + x_0)^2$ versus t, which is related to the experimental constant K_I and the entrainment coefficient.

We should point out that for the planar gravity currents on a slope, as indicated by [13], the planar gravity currents may take only part of the total buoyancy in the lock and carry it into the deceleration phase. The fraction of the total buoyancy which is taken by the planar gravity currents into the deceleration phase could also be estimated experimentally and theoretically, as done by [8]. The central idea, which makes the estimation of the fraction of the total buoyancy in the deceleration phase possible theoretically, is that the entrainment coefficient for the planar gravity currents was estimated geometrically and was independent of the constant K_B in [8]. In other words, K_B for the planar gravity currents is known *a priori*. Therefore, via the measured slope K_M, cf. (1.6) in [8], and K_B, we may estimate the fraction of the total buoyancy taken into the deceleration phase for the planar gravity currents.

However, in our case the gravity currents on laterally unbounded uniform slopes, the shape may vary as the gravity currents propagate on the slope and the entrainment coefficient in the wedge integral model is essentially a combination of the entrainment coefficients over the top and front areas, as explained above. As such, we are not in a good position to determine the entrainment coefficient in our case as a priori. In fact, K_I in our study is a function of the entrainment coefficient. We calculate K_I using (9) based on the measured slope and the total buoyancy and use (10) to calculate the entrainment coefficient once K_I is known. Since the entrainment coefficient in our study is not independent of K_I, it seems not likely to estimate the fraction of the total buoyancy carried into the deceleration phase for the gravity currents on unbounded uniform slopes. In the literature, as also done in [44], the value of the entrainment coefficient was chosen such that the wedge integral model, with total buoyancy in the gravity currents, best describes the front location history. In order to compare our results with [44], including both K_I and α, here we adopt the total buoyancy in (9) and use (10) to calculate the entrainment coefficient. We could have assumed that only a fraction of the total buoyancy is taken into the deceleration phase and, consequently, the entrainment coefficient would take smaller values. But at this stage we do not have sufficient density field information to determine the fraction of the total buoyancy which is taken into the deceleration phase for the gravity currents on unbounded uniform

slopes. We should keep in mind that assuming the gravity currents carrying the total buoyancy into the deceleration phase in our study is a first-order approximation.

We should also remark that the wedge integral model is based on the turbulent entrainment assumption, which appears to be appropriate for the gravity currents on 12°, 9°, 6° unbounded uniform slopes in our study. Strictly speaking, the wedge integral model is not appropriate for the gravity currents on 3° unbounded uniform slope and unbounded horizontal boundary in our study. Although, based on the scaling arguments, the front location history for the gravity currents on 3° unbounded uniform slope and unbounded horizontal boundary similarly follows (9) when the buoyancy and inertia forces are in balance, we should not use (10) to compute the entrainment coefficients.

The wedge integral model includes the buoyancy force and inertia force and the asymptotic relationship (9) is essentially a statement of balance between these two forces. Using the scaling arguments similar to [8, 17], the buoyancy force per unit volume of the wedge scales as $\rho_0 B(x_f + x_0)^{-3}$ and the inertia force scales as $\rho_0(x_f + x_0)t^{-2}$. Therefore, when a balance between the buoyancy force and inertia force is reached, the front location history follows the power-relationship (9) and we shall term this time period the early stage of the deceleration phase.

In this study, we found for the first time that for the gravity currents on unbounded uniform slopes there exists a late stage of the deceleration phase during which the viscous force becomes more important. Here we provide a scaling analysis to describe the front location history in the late stage of the deceleration phase. In the late stage of the deceleration phase, the viscous force per unit volume scales as $\rho_0 \nu(x_f + x_0)t^{-1}\delta^{-1}V_0^{-1/3}$, where the viscous stress is estimated as $\rho_0 \nu(x_f + x_0)t^{-1}\delta^{-1}$, the thickness of the boundary layer at the edge of the current is estimated as $\delta \sim (\nu t)^{1/2}$ and $V_0^{1/3}$ is an estimate for the length scale for the 'active' current head. As will be shown later in more detail, for the gravity currents propagating on an unbounded uniform slope equal to and greater than 6°, an 'active' current head separates from the body in the late deceleration phase and leaves an 'inactive' body of the current behind. Therefore, when a balance between the buoyancy force and viscous force is reached for the 'active' current head, the following relationship applies in the late deceleration phase, i.e.

$$(x_f + x_0)^{8/3} = K_{VS}\left(\frac{B^2 V_0^{2/3}}{\nu}\right)^{1/3}(t + t_{VS}), \tag{11}$$

where K_{VS} is an experimental constant and t_{VS} is the t-intercept. The experimental constant K_{VS} needs to be determined by the measured slope in the plot of $(x_f + x_0)^{8/3}$ versus t in the late stage of the deceleration phase. As explained above for (9), we do not have control over the t-intercept t_{VS} in (11). The t-intercept t_{VS} is identified by finding the point where (11) crosses the t-axis. We include t_{VS} for completeness as will be shown later in Table 2. We are particularly concerned about the slope in the plot of $(x_f + x_0)^{8/3}$ versus t, which is related to the experimental constant K_{VS} and is a strong evidence showing that the front propagates progressively slower than (9) as time proceeds.

For the gravity currents propagating on an unbounded uniform slope equal to and less than 3°, the gravity currents maintain an integrated shape throughout the motion and the separation process of an 'active' head for the gravity currents propagating on a slope equal to and greater than 6° does not exist. In the early stage of the deceleration phase when the buoyancy and inertia forces are in balance, based on the scaling arguments, the front location history similarly follows the relationship (9). In the late stage of the deceleration phase

when the buoyancy and viscous forces are in balance, the front location history follows the power-relationship

$$(x_f + x_0)^4 = K_{VM}\left(\frac{B^2 V_0^2}{\nu}\right)^{1/3}(t + t_{VM}), \tag{12}$$

where K_{VM} is an experimental constant and t_{VM} is the t-intercept. The scaling analysis is based on the fact that the gravity currents maintain an integrated shape throughout the motion. Here the viscous stress is applied over the whole top area, which is estimtated as being proportional to $(x_f + x_0)^2$. The experimental constant K_{VM} needs to be determined by the measured slope in the plot of $(x_f + x_0)^4$ versus t in the late stage of the deceleration phase. Similarly, we do not have control over the t-intercept t_{VM} in (12). The t-intercept t_{VM} is identified by finding the point where (12) crosses the t-axis and is included for completeness in Table 3. We are concerned about the slope in the plot of $(x_f + x_0)^4$ versus t, which is related to the experimental constant K_{VM} and is also a strong evidence showing that the front propagates progressively slower than (9) as time proceeds. Encouragingly, the power-relationship (12) is consistent with that originally proposed by [17] for the gravity currents propagating radially outward on an unbounded horizontal plane in the viscous phase and, as will be shown later, our experimental constant K_{VM} is consistent with the estimate based on [17]. Based on the experiments reported by [17, 18] for the gravity currents on an unbounded horizontal plane in the inertial phase, the experimental constant K_I in our configuration can be estimated as 5.71 and 3.62, respectively. Furthermore, based on the experiments reported by [17] for the gravity currents on an unbounded horizontal plane in the viscous phase, the experimental constant K_{VM} in our configuration can be estimated as 1.24. It is reasonable to expect that the gravity currents propagating on a 3° unbounded uniform slope and on an unbounded horizontal boundary behave similarly and the power-relationship (12) applies in the late stage of the deceleration phase.

3 Experimental setup

A sketch of the tank, with top and side views, used in the experiments is provided in Fig. 1. The rectangular tank has dimensions of 1.6 m in width, 0.6 m in depth and 2.5 m in length. For visualization purposes, all four sides were constructed by transparent Perspex walls fitted in a reinforced steel frame. A Perspex board with dimensions of 2.47 m in length and slightly less than 1.6 m in width was installed near the bottom of the tank to act as an unbounded uniform slope, of which the slope angle can be adjusted in the range of $0° \le \theta \le 12°$. The Perspex board was reinforced with grid structure at its base to minimize the curvature which might have undesired influence on the propagation of gravity currents.

The lock has dimensions of $b_0 = 10$ cm in width, $h_0 = 8$ cm in height and $l_0 = 10$ cm in length and was mounted on the upslope end of the Perspex board. One side of the lock, facing the downslope end of the sloping bottom, is slidable and can be easily withdrawn from the lock. Two holes with diameter of 1/4 in were drilled and tapped on the back of the lock to allow injection of heavy fluid into and escape of trapped air from the lock. The lock was submerged beneath the surface of ambient fluid by more than 10 cm to reduce the influence due to the free surface. The heavy fluid in the lock was set into motion when the gate was removed from the lock.

To aid flow visualization, potassium permanganate was added in the heavy fluid. Two uniform LED light boards and light-diffusing screens were placed against both the upslope and downslope walls of the tank to provide illumination. To record video of the propagation of gravity currents, a Sony HDR-PJ670 was positioned 4 m above the free surface of ambient fluid for the top views and a Canon EOS 700D was positioned at about 4 m away from the side wall of the tank for the side views of the gravity currents. Both cameras have spatial and temporal resolutions of 1920×1080 at 24 frames per second. The Canon EOS 700D camera was rotated at the same angle as the bottom slope such that the x and y axes in the images align with the downslope and wall-normal directions. A distance of 250.00 cm along the slope in the tank corresponds to about 1000 pixels in the images, so each pixel in the downslope direction represents 0.25 cm approximately. The recorded videos of the gravity currents were exported to a PC for postprocessing.

In the experiments, sodium chloride solution was chosen as the heavy fluid while tap water was chosen as the ambient fluid. The kinematic viscosity of the sodium chloride solution is taken to be the same as the tap water as $\nu = 1.1 \times 10^{-2}$ cm^2 s^{-1}. Densities of the heavy fluid and ambient fluid were measured by KEM DA-130N density meter with an accuracy of 10^{-3} g cm^{-3} and maintained at $\rho_1 = 1.015 \pm 0.001$ g cm^{-3} and $\rho_0 = 0.998 \pm 0.001$ g cm^{-3}, respectively. The reduced gravity $g_0' = g(\rho_1 - \rho_0)/\rho_0$ was approximately $g_0' \approx 16.71$ cm s^{-2} and the Reynolds number $\mathrm{Re} = \sqrt{g_0' h_0 h_0}/\nu \approx 8500$ was far in excess of 1000, above which the viscous effects were thought to be negligible compared with the inertial effects [46].

4 Results

In the following we shall present the results for the gravity currents produced from a finite volume of heavy fluid propagating on unbounded uniform slopes $\theta = 12°, 9°, 6°, 3°, 0°$ in order. The dimensions of the lock and the densities of the heavy fluid and ambient fluid were maintained unchanged throughout the experiments. On each slope angle, at least five repeated runs were performed in order to make qualitative and quantitative observations. Other experimental parameters are listed in Table 1.

4.1 Gravity currents propagating on a 12° slope

4.1.1 Qualitative features

The flow morphology of the gravity current propagating on a 12° slope is shown from the top view in Fig. 2 and from the side view in Fig. 3. After the gate is removed, the heavy fluid immediately spreads outward from the lock, as shown in Figs. 2 and 3 at $t = 2$, 6 s. Afterwards, the gravity current takes a wedge shape, of which the thickness increases towards the front of the current, as shown in Figs. 2 and 3 at $t = 10$, 20 s. Our qualitative observation on the shape of the gravity current is consistent with the wedge or boomerang shape reported previously [44, 52]. In the top view images, we can also observe the undulations occurring around the edge of the gravity current as the lobe and cleft structure. Once the wedge shape is formed, the gravity current continues to propagate on the slope while maintaining the wedge shape, as shown in Figs. 2 and 3 at $t = 30$ s. The width and height of the wedge progressively increase as the gravity current propagates downslope. However, the gravity current maintains its integrated shape only for a limited period of time. As

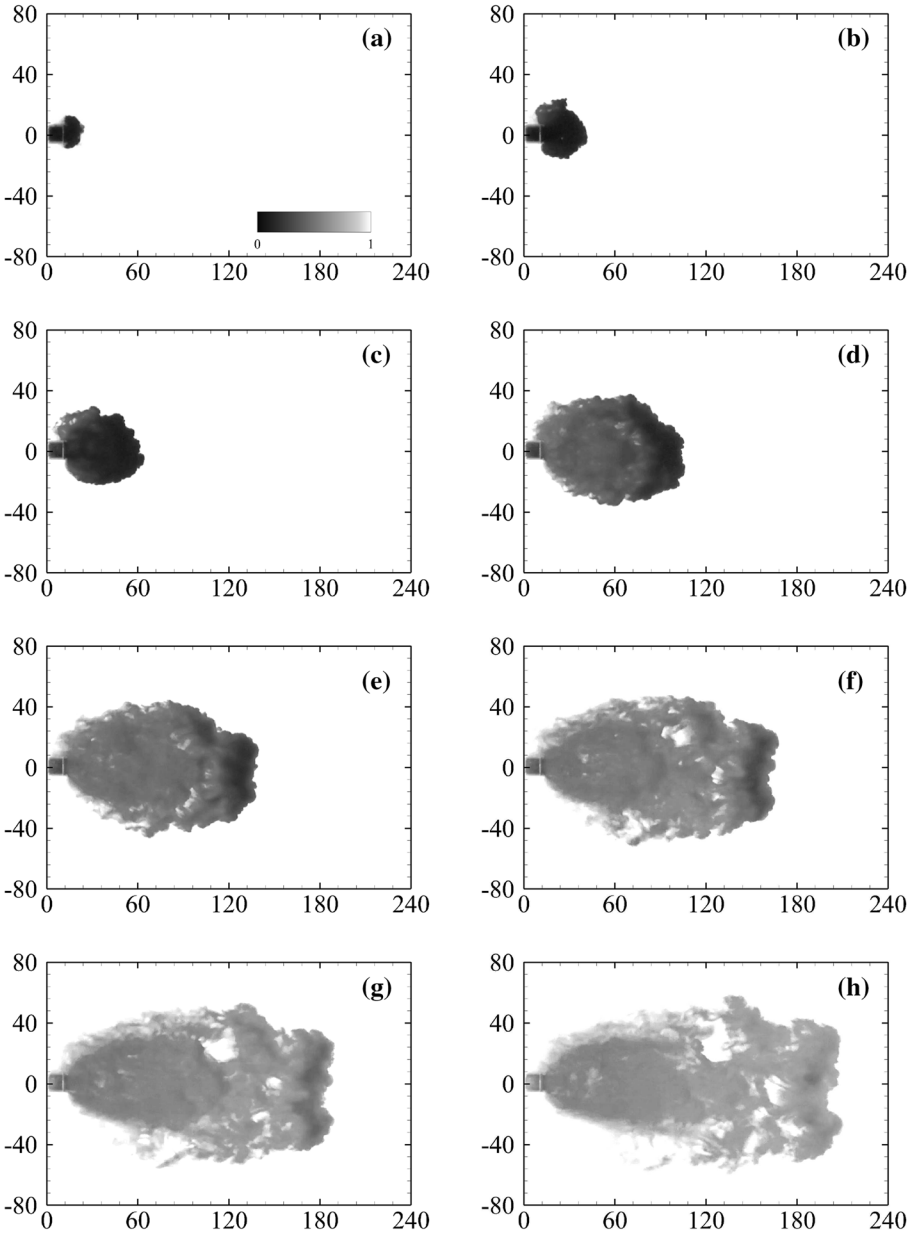

Fig. 2 Experiment 12/21/16-1: top view images for the gravity current propagating on a 12° unbounded uniform slope. The reduced gravity in this experiment was $g_0' = 17.10$ cm s^{-2}. Distances in the downslope and spanwise directions are in units of cm. Time instances are chosen at (**a**–**h**) $t = 2$, 6, 10, 20, 30, 40, 50, 60 s

shown in Fig. 2 at $t = 40$, 50, 60 s, bare regions as represented by the white patches emerge as the gravity current propagates further downslope. Figure 3 at $t = 40$, 50, 60 s also shows that an 'active' part of the head becomes disintegrated from the body of the current. While

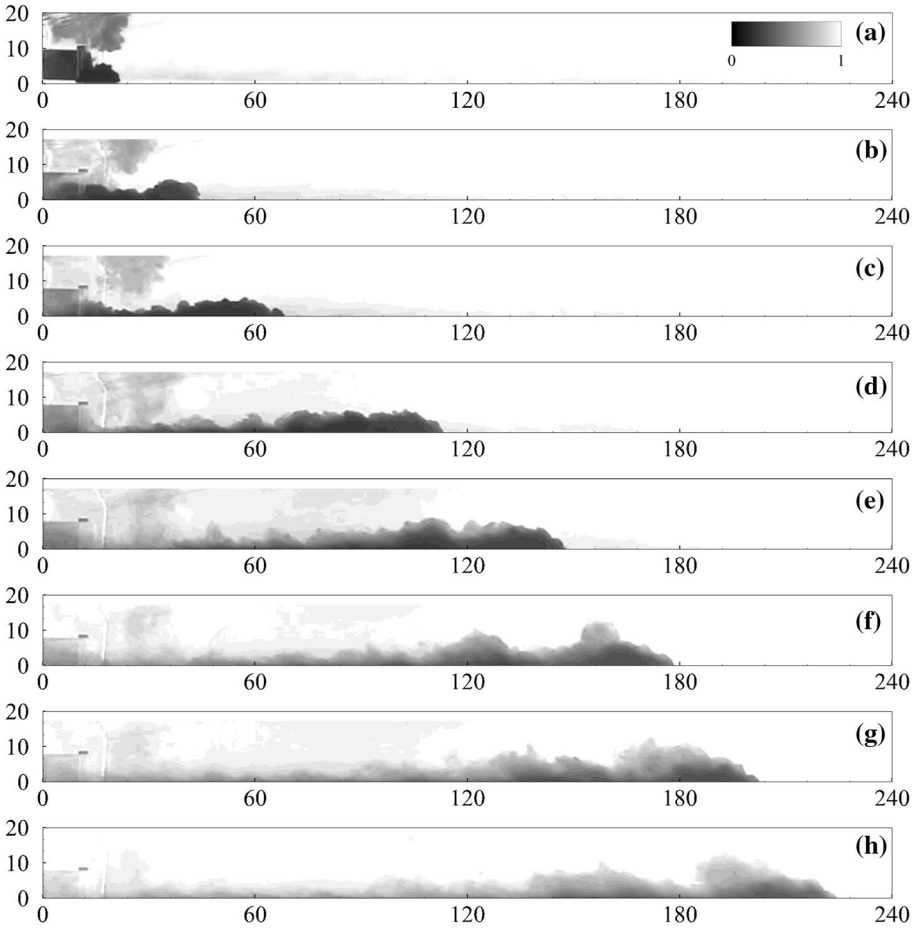

Fig. 3 Experiment 12/21/16-1: side view images for the gravity current propagating on a 12° unbounded uniform slope as shown in Fig. 2. Distances in the downslope and wall-normal directions are in units of cm. Time instances are chosen at (**a**–**h**) $t = 2$, 6, 10, 20, 30, 40, 50, 60 s

Table 1 Table showing the operational parameters, including the slope angle θ, reduced gravity g_0', time t_{max} and front location $x_{f_{max}}$, measured from the lock gate, at which the gravity currents reach the maximum front velocity $U_{f\,max}$

θ	g_0' (cm s^{-2})	t_{max} (s)	$x_{f\,max}$ (cm)	$U_{f\,max}$ (cm s^{-1})
12°	$17.02^{+0.12}_{-0.05}$	$7.16^{+1.66}_{-1.99}$	$35.29^{+8.95}_{-10.79}$	$6.13^{+1.35}_{-0.53}$
9°	$17.12^{+0.09}_{-0.18}$	$5.03^{+1.63}_{-1.03}$	$26.65^{+9.85}_{-8.90}$	$6.60^{+0.23}_{-0.34}$
6°	$17.05^{+0.20}_{-0.15}$	$5.19^{+0.63}_{-0.52}$	$26.37^{+2.87}_{-3.62}$	$6.59^{+0.47}_{-0.21}$
3°	$17.11^{+0.18}_{-0.14}$	$3.94^{+1.38}_{-0.94}$	$18.12^{+6.62}_{-3.37}$	$6.61^{+0.66}_{-0.56}$
0°	$17.06^{+0.21}_{-0.17}$	$3.64^{+0.85}_{-1.14}$	$15.16^{+3.58}_{-4.66}$	$6.39^{+0.41}_{-0.34}$

Each value is the average of five experiments. The error estimates are to add and subtract the maximum and minimum values and are not the r.m.s. estimates

the edge of the 'active' head is uplifted and engulfed by the ambient fluid, the 'inactive' body of the current moves more slowly. Our observation on the separation of the 'active' head from the body of the current is persistent at the later stage of propagation for all the gravity currents on a 12° slope and is reported in this study for the first time. Such an observation on the gravity current on a 12° unbounded uniform slope is qualitatively similar to the flow morphology of the planar gravity currents propagating on 6° and 9° slopes in the late deceleration phase. As reported by [8], for the planar gravity currents on 6° and 9° slopes, the edge of the gravity current head experiences a large upheaval and enrolment by the ambient fluid towards the end of the deceleration phase.

4.1.2 Quantitative results

From the top view images of the gravity current as shown in Fig. 2, the front location can be identified without ambiguity. Specifically, we put a grid on the top view images in post-processing and the front location is defined as the furthest streamwise location reached by the gravity current. The front velocity can be calculated as the time rate of change of the front location. Although the detailed structure of the gravity currents between runs may differ due to different turbulent evolutions, the features as observed and reported for the front location history and front velocity history are persistent. Figure 4 shows the front location and front velocity histories for the gravity current propagating on a 12° slope. From the front velocity history, it is observed that the first acceleration phase begins when the heavy fluid is released from the lock and the first acceleration phase ends at $t \approx 1.0$ s. The second acceleration phase, beginning at $t \approx 2.0$ s, ends at $t \approx 6.83$ s when a maximum front velocity $U_{f_{max}} \approx 5.73$ cm s^{-1} is reached. Our observation on the two consecutive acceleration phases following the release of heavy fluid on a 12° slope is persistent for all runs. Interestingly, [52] also reported the two consecutive acceleration phases for the gravity currents on a range of slope angles between 5° and 20°, albeit with a lock configuration which is designed differently from our experimental setup.

Our focus in this study is on the deceleration phase of propagation. After $t \approx 6.83$ s, the gravity current moves into the deceleration phase and we shall examine the front location history in the deceleration phase in detail according to (9) and (11). We plot the front

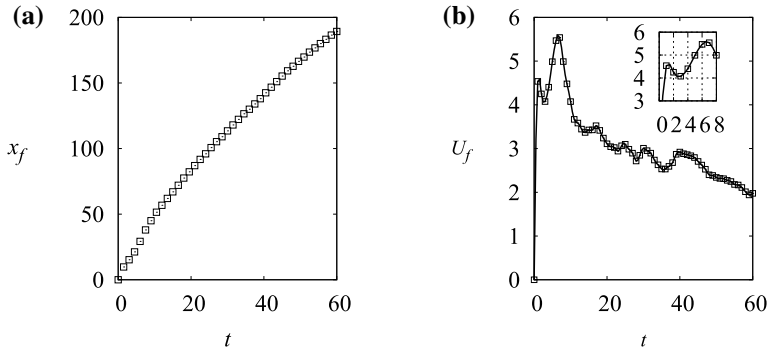

Fig. 4 Experiment 12/21/16-1: front location history (**a**) and front velocity history (**b**) for the gravity current propagating on a 12° unbounded uniform slope. The reduced gravity in this experiment was $g'_0 = 17.10$ cm s^{-2}. The maximum front velocity $U_{f_{max}} \approx 5.73$ cm s^{-1} occurs at $t \approx 6.83$ s. The front location is in units of cm, front velocity is in units of cm s^{-1} and time is in units s

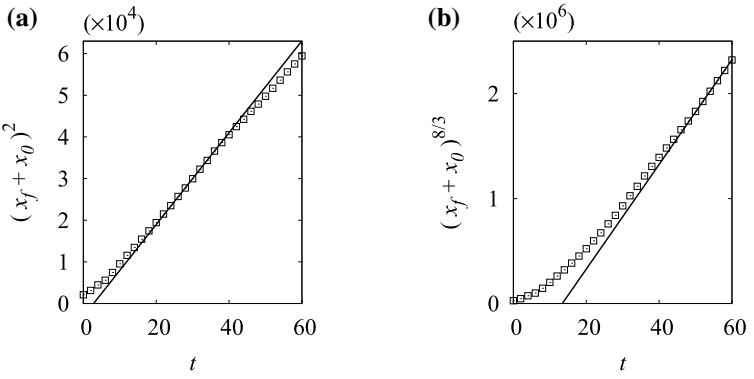

Fig. 5 Experiment 12/21/16-1: relationship between **a** $(x_f + x_0)^2$ and t and **b** $(x_f + x_0)^{8/3}$ and t for the gravity current propagating on a 12° unbounded uniform slope. The reduced gravity in this experiment was $g_0' = 17.10$ cm s^{-2}. The front location is in units of cm and time is in units of s. The solid line in **a** represents the straight line of best fit to the early deceleration phase and the fitting equation is $(x_f + x_0)^2 = \left(K_I B\right)^{1/2}(t + t_I)$, where $K_I = 88.88$, $B = 13{,}680$ cm^4 s^{-2}, $x_0 = 45.83$ cm and $t_I = -2.80$ s. The solid line in **b** represents the straight line of best fit to the late decelearation phase and the fitting equation is $(x_f + x_0)^{8/3} = K_{VS} B^{2/3} V_0^{2/9} \nu^{-1/3}(t + t_{VS})$, where $K_{VS} = 4.25$ and $t_{VS} = -13.43$ s. The maximum front velocity $U_{f\,max} \approx 5.73$ cm s^{-1} occurs at $t \approx 6.83$ s

Table 2 Table showing the dependent variables for the gravity currents propagating on 12°, 9°, 6° slopes, including the entrainment coefficient α, distance from the virtual origin to the lock gate x_0, experimental constant K_I, t-intercept t_I in (9), experimental constant K_{VS} and t-intercept t_{VS} in (11)

θ	α	x_0 (cm)	K_I	t_I (s)	K_{VS}	t_{VS} (s)
12°	$0.164^{+0.005}_{-0.017}$	$45.44^{+4.56}_{-5.44}$	$92.99^{+5.75}_{-5.02}$	$-2.21^{+8.84}_{-5.67}$	$4.43^{+0.78}_{-1.01}$	$-11.88^{+5.06}_{-2.95}$
9°	$0.174^{+0.003}_{-0.002}$	$48.37^{+3.27}_{-4.38}$	$79.78^{+2.41}_{-3.93}$	$0.22^{+0.89}_{-0.91}$	$4.09^{+0.08}_{-0.07}$	$-11.39^{+5.01}_{-5.81}$
6°	$0.204^{+0.014}_{-0.007}$	$50.31^{+6.62}_{-3.82}$	$57.52^{+4.23}_{-8.03}$	$2.75^{+2.46}_{-2.01}$	$2.99^{+0.22}_{-0.23}$	$-3.88^{+10.25}_{-7.39}$

The subscripts *I* and *VS* represent the inertial phase and viscous phase for the gravity currents on 12°, 9°, 6° slopes, respectively

location history in terms of $(x_f + x_0)^2$ versus t in Fig. 5a and $(x_f + x_0)^{8/3}$ versus t in Fig. 5b. Here $(x_f + x_0)$ represents the front location measured from the virtual origin, which can be identified by extrapolating the development of the width of the wedge in the upslope direction. In the early stage of the deceleration phase, Fig. 5a reveals that the front location history robustly follows the power-relationship (9) during $20 \lesssim t \lesssim 40$ s. The application of the power-relationship (9) in the early stage of the deceleration phase suggests a balance between the buoyancy and inertia forces, as predicted by the integral model and by the scaling analysis. It is worth noting that in the early stage of the deceleration phase, the gravity current propagates downslope while still maintaining an integrated wedge shape. The straight line of best fit to the early deceleration phase is shown in Fig. 5a and the fitting equation is $(x_f + x_0)^2 = \left(K_I B\right)^{1/2}(t + t_I)$, where $K_I = 88.88$, $B = 13680$ cm^4 s^{-2}, $x_0 = 45.83$ cm and $t_I = -2.80$ s. Here the experimental constant K_I is calculated according to (9) and based on the slope of the best fit to the early deceleration phase and the total buoyancy in the experiment. With the help of (10), we may also calculate the entrainment coefficient $\alpha = 0.165$. The experimental constant K_I along with other variables for

the gravity currents propagating on 12°, 9° and 6° slopes are listed in Table 2. However, as shown in Fig. 5a, the front location history follows (9) only for a limited period of time. When $t \gtrsim 40$ s, the front location history begins to deviate from the power-relationship (9) and, when the deviation occurs, the front Reynolds number based on the front velocity and front thickness, $\mathrm{Re}_f = U_f h/\nu$, is about $\mathrm{Re}_f \approx 3000$.

In the late stage of the deceleration phase, Fig 5b reveals that the front location history follows the power-relationship (11) during $t \gtrsim 40$ s. The application of the power-relationship (11) in the late deceleration phase suggests a balance between the buoyancy and viscous forces, as argued by the scaling analysis. It is worth noting that, in the late stage of the deceleration phase, the gravity current begins to disintegrate into an 'active' part which is engulfed by the ambient fluid and the 'inactive' body of the current which moves on the slope more slowly. The equation of the straight line of best fit to the late deceleration phase is $(x_f + x_0)^{8/3} = K_{VS} B^{2/3} V_0^{2/9} \nu^{-1/3} (t + t_{VS})$, where $K_{VS} = 4.25$ and $t_{VS} = -13.43$ s. The experimental constant K_{VS}, as listed in Table 2, is calculated according to (11) and based on the slope of the best fit to the late deceleration phase and other relevant parameters in (11).

4.2 Gravity currents propagating on 9° and 6° slopes

Gravity currents propagating on 9° and 6° slopes are qualitatively similar to the gravity currents propagating on a 12° slope. For a concise presentation, we show the gravity current on a 6° slope for illustrative purposes and the readers are referred to Tables 1 and 2 for other quantitative measures.

Figure 6 shows the top view images for the gravity current on a 6° slope. The front velocity history, computed based on the front location history, is shown in Fig. 7. After released from the lock, the heavy fluid initially spreads outward and the gravity current takes the wedge shape. According to the front velocity history, the gravity current propagating on 9° (not shown) and 6° slopes also exhibit two consecutive acceleration phases. As listed in Table 2, the maximum front velocities reached at the end of the second acceleration phase on different slopes show significant scatter. The average maximum front velocities on 9° and 6° slopes are slightly greater than the average maximum front velocity on a 12° slope but their difference is about on the same order as the error estimates. After the second acceleration phase, the gravity current moves into the early stage of the deceleration phase while maintaining an integrated wedge shape. In the late stage of the deceleration phase, the disintegration of an 'active' head from the body of the current occurs persistently for the gravity currents on 9° and 6° slopes. We may examine the front location history for the gravity currents on 9° (not shown) and 6° slopes in the early and late stages of the deceleration phase according to (9) and (11), as shown in Fig. 8.

Based on the slope of the best fit line to the early deceleration phase in Fig. 8a, we may calculate the experimental constant $K_I = 56.29$ and the entrainment coefficient $\alpha = 0.205$. [44] showed that the wedge integral model well describes the front location history and we may plot their front location history in terms of (9) and calculate the corresponding values of K_I, as shown in Fig. 9. Our reported values of K_I agree with those values based on the experiments of [44] and the experimental constant K_I increases as the slope angle increases. The application of (9) in both the experiments of [44] and ours suggests that a balance between the buoyancy and inertia forces is reached in the early stage of the deceleration phase even though the lock configurations in the two experimental setups are different. The entrainment coefficient α is found to weakly depend on the slope and is consistent

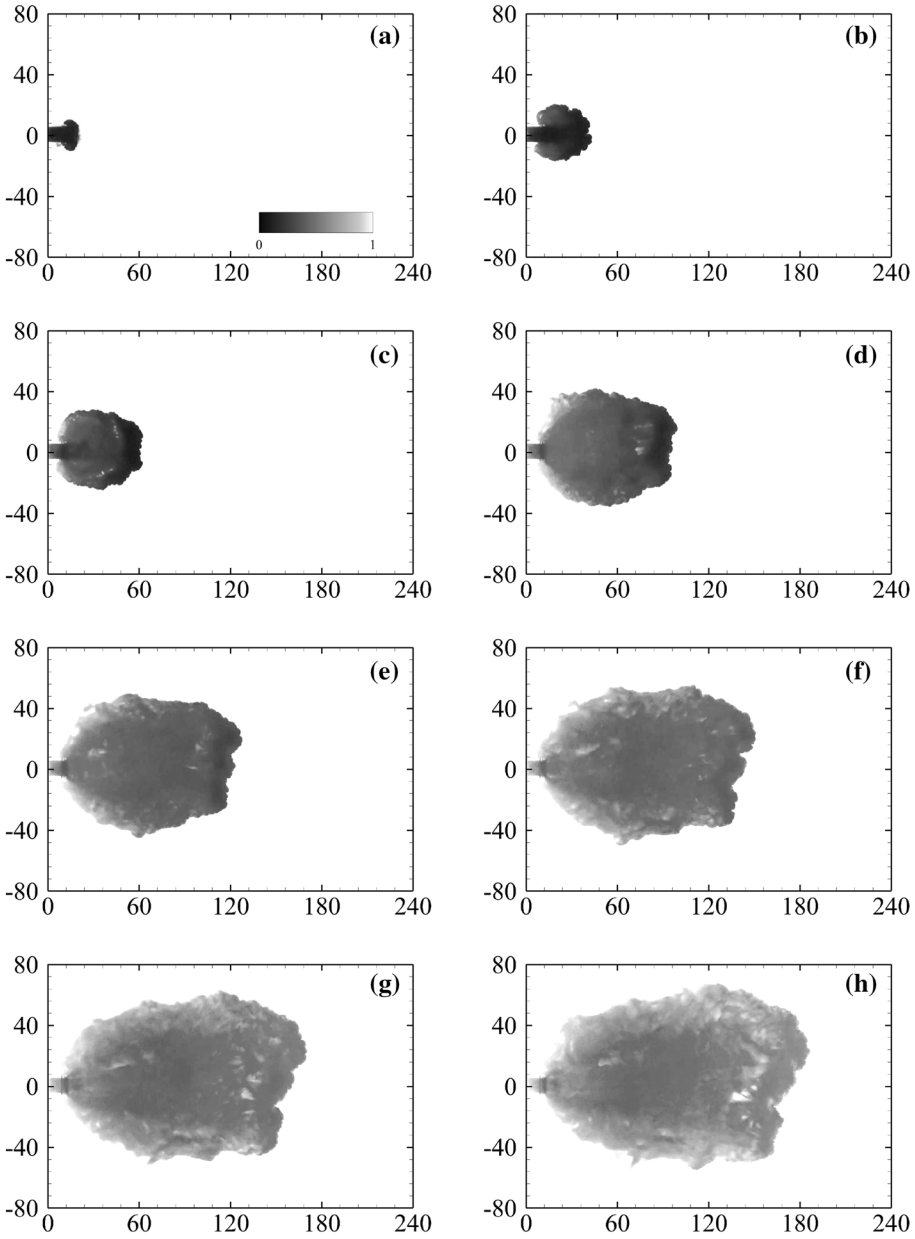

Fig. 6 Experiment 08/30/16-1: top view images for the gravity current propagating on a 6° unbounded uniform slope. The reduced gravity in this experiment was $g_0' = 17.20$ cm s^{-2}. Distances in the downslope and spanwise directions are in units of cm. Time instances are chosen at (**a**–**h**) $t = 2$, 6, 10, 20, 30, 40, 50, 60 s

with the reported values given by [44] and [52], as shown in Fig. 10. In order to compare our results with [44], the experimental constant K_I and the entrainment coefficient α are calculated using the total buoyancy in (9). As explained above, the gravity currents may

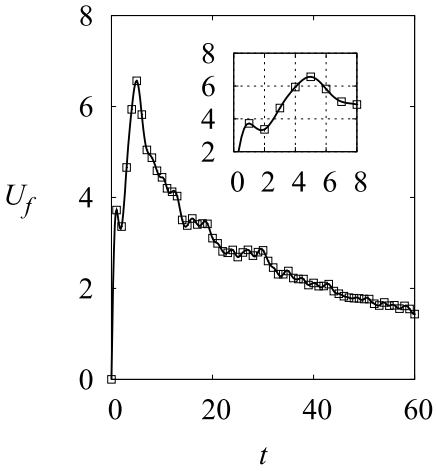

Fig. 7 Experiment 08/30/16-1: front velocity history for the gravity current propagating on a 6° unbounded uniform slope. The reduced gravity in this experiment was $g_0' = 17.20$ cm s^{-2}. The maximum front velocity $U_{f_{max}} \approx 6.56$ cm s^{-1} occurs at $t \approx 5.0$ s. The front velocity is in units of cm s^{-1} and time is in units of s

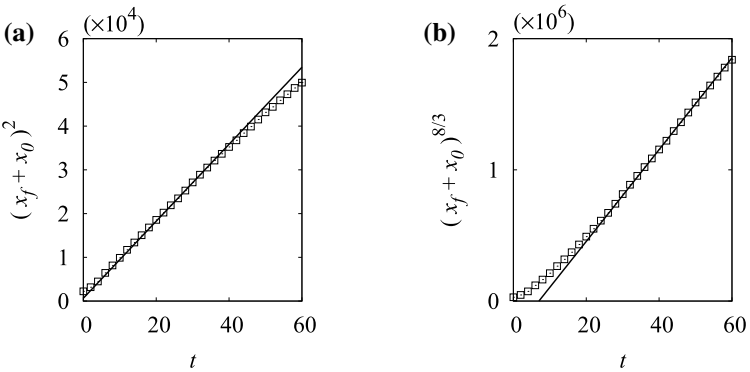

Fig. 8 Experiment 08/30/16-1: relationship between **a** $(x_f + x_0)^2$ and t and **b** $(x_f + x_0)^{8/3}$ and t for the gravity current propagating on a 6° unbounded uniform slope. The reduced gravity in this experiment was $g_0' = 17.20$ cm s^{-2}. The front location is in units of cm and time is in units of s. The solid line in **a** represents the straight line of best fit to the early deceleration phase and the fitting equation is $(x_f + x_0)^2 = \left(K_I B\right)^{1/2}(t + t_I)$, where $K_I = 56.29$, $B = 13760$ cm^4 s^{-2}, $x_0 = 47.23$ cm and $t_I = 0.74$ s. The solid line in **b** represents the straight line of best fit to the late decelearation phase and the fitting equation is $(x_f + x_0)^{8/3} = K_{VS} B^{2/3} V_0^{2/9} \nu^{-1/3}(t + t_{VS})$, where $K_{VS} = 2.97$ and $t_{VS} = -7.00$ s. The maximum front velocity $U_{f_{max}} \approx 6.56$ cm s^{-1} occurs at $t \approx 5.0$ s

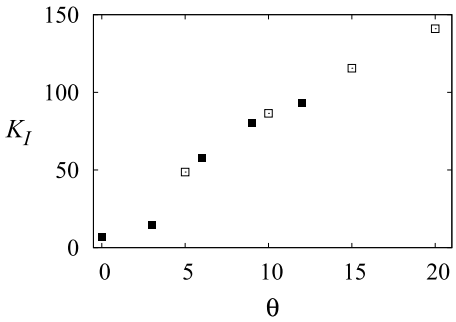

Fig. 9 Experimental constant K_I as a function of the slope angle θ. Symbols: filled square, present experiments; opened square, K_I values based on the front location histories reported by [44]

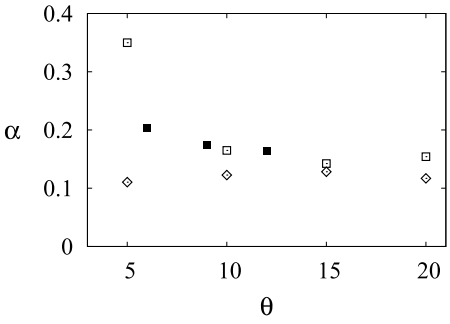

Fig. 10 Entrainment coefficient α as a function of the slope angle θ. Symbols: filled square, present experiments; opened square, values reported by [44]; diamond, values reported by [52]

not take the full charge of the total buoyancy into the deceleration phase, but currently we do not have sufficient density field information to quantify the fraction of the total buoyancy carried into the deceleration phase by the gravity currents on unbounded uniform slopes. As assumed by the wedge integral model, the gravity currents propagating on 6°, 9°, 12° slopes maintain a wedge shape in the early stage of the deceleration phase and, consequently, we may use (10) to calculate the entrainment coefficient. As will be shown later, the gravity currents propagating on a 3° slope and on a horizontal boundary do not take the wedge shape neither in the early stage nor in the late stage of the deceleration phase. Although the front location history similarly follows (9) in the early deceleration phase, it is not appropriate to use (10) to calculate the entrainment coefficient for the gravity currents on a 3° slope and on a horizontal boundary.

In the late stage of the deceleration phase, the front location history begins to deviate from the power-relationship (9) at $t \approx 40$ s and the power-relationship (11) applies. When the front location history begins to deviate from the power-relationship (9), the front Reynolds number is about $\mathrm{Re}_f \approx 2000$. Based on the slope of the best fit line in Fig. 8b and (11), we may calculate the experimental constant $K_{VS} = 2.97$. As listed in Table 2, the experimental constant K_{VS} decreases as the slope angle decreases. When compared with the gravity current on a 12° slope, the area of white spots is reduced for the gravity current propagating on a 6° slope in the late deceleration phase, as shown in Fig. 6 for $t \gtrsim 40$ s. Such an observation suggests that, when the slope angle decreases, the flow morphology approaches towards that of the gravity currents on a 3° slope and on a horizontal boundary.

4.3 Gravity currents on a 3° slope

Gravity currents propagating on a 3° slope are qualitatively different from the gravity currents on the 12°, 9° and 6° unbounded uniform slopes, from a number of perspectives. After released from the lock, the heavy fluid spreads outward continuously, as shown by the top view images in Fig. 11. Furthermore, for the gravity current on a 3° slope, there is no bare region appearing inside the heavy fluid, even in the late deceleration phase for $t \gtrsim 40$ s. As also shown by the side view images in Fig. 12, the gravity current thickness is more uniform in the streamwise direction. Contrary to the gravity currents on the 12°, 9° and 6° unbounded uniform slopes taking a wedge shape in the early deceleration phase and an 'active' head separated from the body of the current in the late deceleration phase, the gravity current on a 3° slope maintains an integrated shape, which is more akin to a circular disk, throughout the motion. Our observation on the flow morphology of the gravity current on a 3° slope is qualitatively similar to the planar gravity currents on 0° and 2° slopes

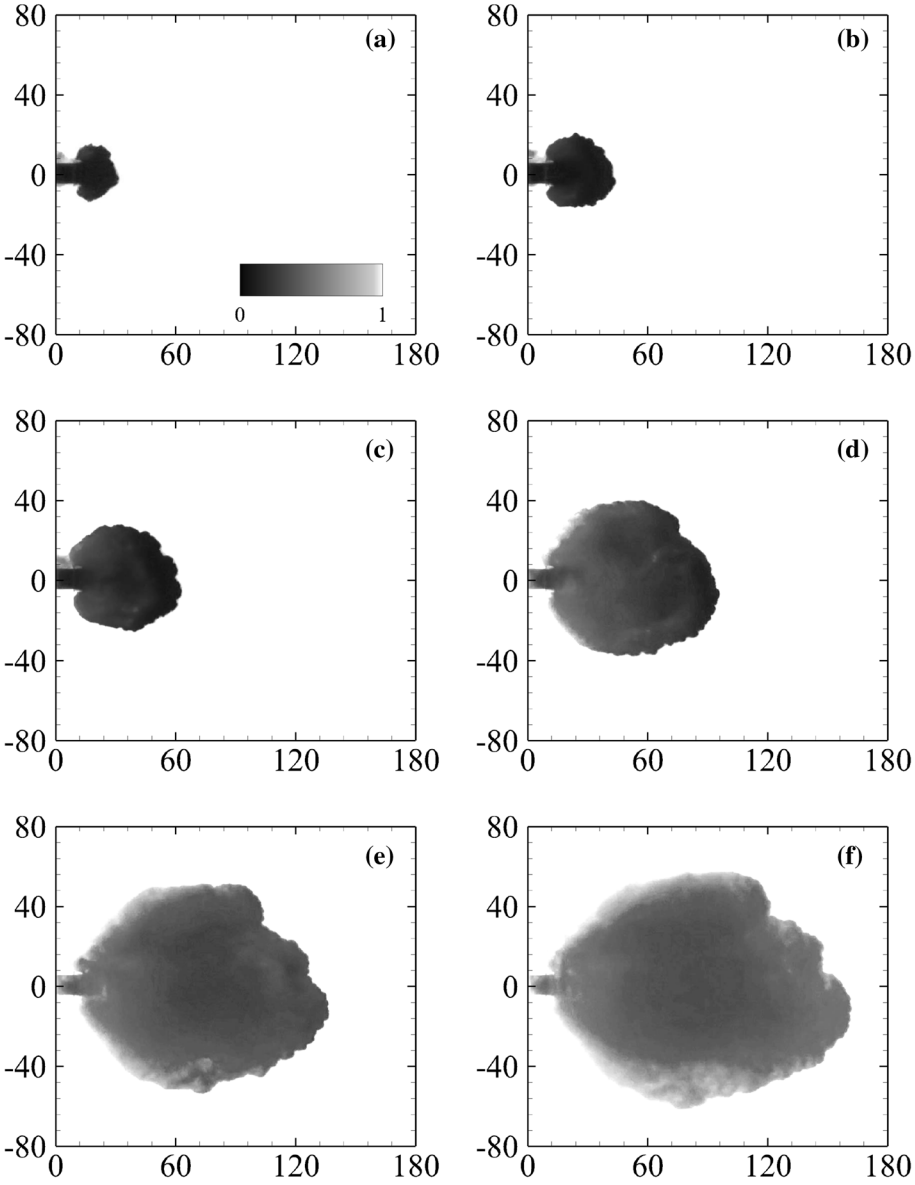

Fig. 11 Experiment 11/28/16-4: top view images for the gravity current propagating on a 3° unbounded uniform slope. The reduced gravity in this experiment was $g_0' = 17.03$ cm s^{-2}. Distances in the downslope and spanwise directions are in units of cm. Time instances are chosen at **a**–**f** $t = 4$, 6, 10, 20, 40, 60 s

in the late deceleration phase. As reported by [8], for the planar gravity currents on 0° and 2° slopes, the gravity current head maintains a more streamlined shape without violent mixing with the ambient fluid throughout the course of propagation.

Figure 13 shows the front velocity history for the gravity current propagating on a 3° slope and there is only one acceleration phase in this case. Such an observation on the

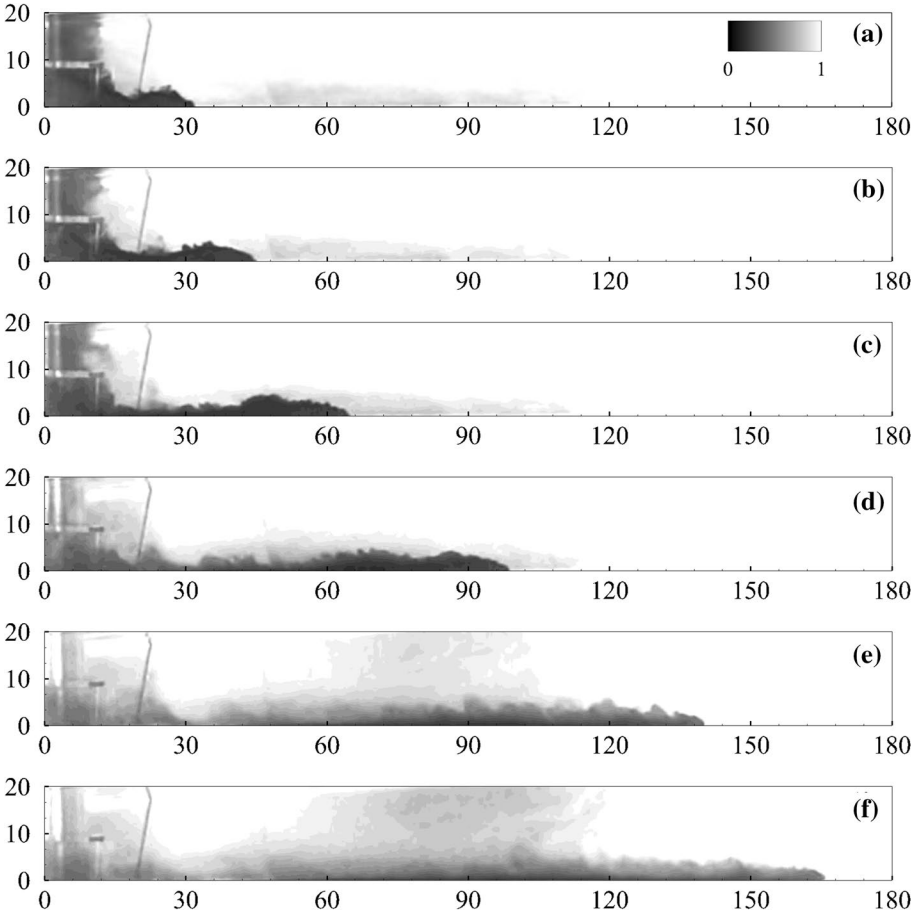

Fig. 12 Experiment 11/28/16-4: side view images for the gravity current propagating on a 3° unbounded uniform slope as shown in Fig. 11. Distances in the downslope and wall-normal directions are in units of cm. Time instances are chosen at **a**–**f** $t = 4$, 6, 10, 20, 40, 60 s

single acceleration phase is similar to that for the gravity current propagating on a horizontal boundary. Following the maximum front velocity, the gravity current moves into the deceleration phase and we may examine the front location history in the early and late stages of the deceleration phase according to (9) and (12).

Figure 14a shows $(x_f + x_0)^2$ versus t and Fig. 14b shows $(x_f + x_0)^4$ versus t. In the early stage of the deceleration phase, Fig. 14a shows that the front location history follows the power-relationship (9) during $10 \lesssim t \lesssim 25$ s. Although the flow morphology of the gravity currents on a 3° unbounded uniform slope is different from that of the gravity currents on the 12°, 9° and 6° unbounded uniform slopes, it is still desirable that there is a balance between the buoyancy and inertia forces and the power-relationship (9) applies in the early stage of the deceleration phase. The straight line of best fit to the early deceleration phase is shown in Fig. 14a and the fitting equation is $(x_f + x_0)^2 = \left(K_I B\right)^{\Gamma/2}(t + t_I)$, where $K_I = 16.41$, $B = 13624$ cm^4 s^{-2}, $x_0 = 9.62$ cm and $t_I = -1.84$ s. As explained above, for the gravity currents on a 3° unbounded uniform

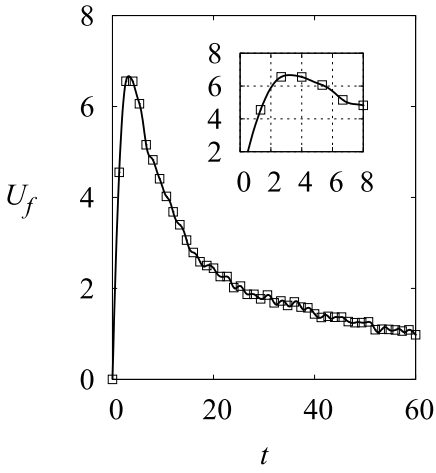

Fig. 13 Experiment 11/28/16-4: front velocity history for the gravity current propagating on a 3° unbounded uniform slope. The reduced gravity in this experiment was $g_0' = 17.03$ cm s^{-2}. The maximum front velocity $U_{f\,max} \approx 6.67$ cm s^{-1} occurs at $t \approx 3.17$ s. The front velocity is in units of cm s^{-1} and time is in units of s

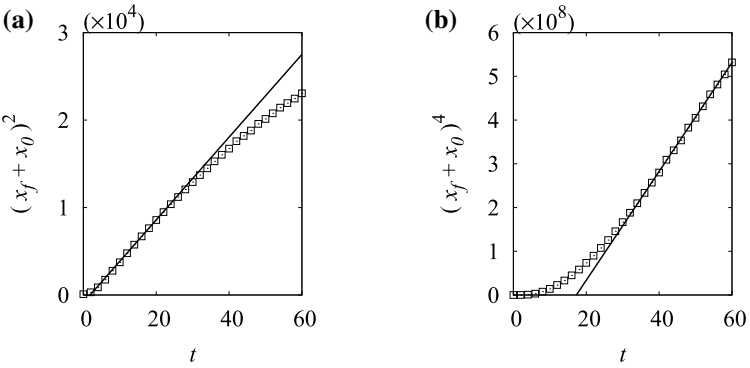

Fig. 14 Experiment 11/28/16-4: relationship between **a** $(x_f + x_0)^2$ and t and **b** $(x_f + x_0)^4$ and t for the gravity current propagating on a 3° unbounded uniform slope. The reduced gravity in this experiment was $g_0' = 17.03$ cm s^{-2}. The front location is in units of cm and time is in units of s. The solid line in **a** represents the straight line of best fit to the early deceleration phase and the fitting equation is $(x_f + x_0)^2 = \left(K_I B\right)^{1/2}(t + t_I)$, where $K_I = 16.41$, $B = 13624$ cm^4 s^{-2}, $x_0 = 9.62$ cm and $t_I = -1.84$ s. The solid line in **b** represents the straight line of best fit to the late decelearation phase and the fitting equation is $(x_f + x_0)^4 = K_{VM} B^{2/3} V_0^{2/3} \nu^{-1/3}(t + t_{VM})$, where $K_{VM} = 54.52$ and $t_{VM} = -17.29$ s. The maximum front velocity $U_{f\,max} \approx 6.67$ cm s^{-1} occurs at $t \approx 3.17$ s

slope and on an unbounded horizontal boundary, the flow morphology is different and it is not appropriate to compute the entrainment coefficient using (10). Again, the front location history for the gravity currents propagating on a 3° unbounded uniform slope follows (9) only for a limited period of time, as shown in Fig. 14a. When $t \gtrsim 25$ s, the front location history begins to deviate from the power-relationship (9) and, when the deviation occurs, the front Reynolds number is about $\mathrm{Re}_f \approx 1000$.

In the late stage of the deceleration phase, Fig. 14b shows that the front location history follows the power-relationship (12) during $t \gtrsim 30$ s. It is worth noting that in the late deceleration phase, the gravity current on a 3° slope maintains an integrated, circular disk shape throughout the motion without the disintegration process observed

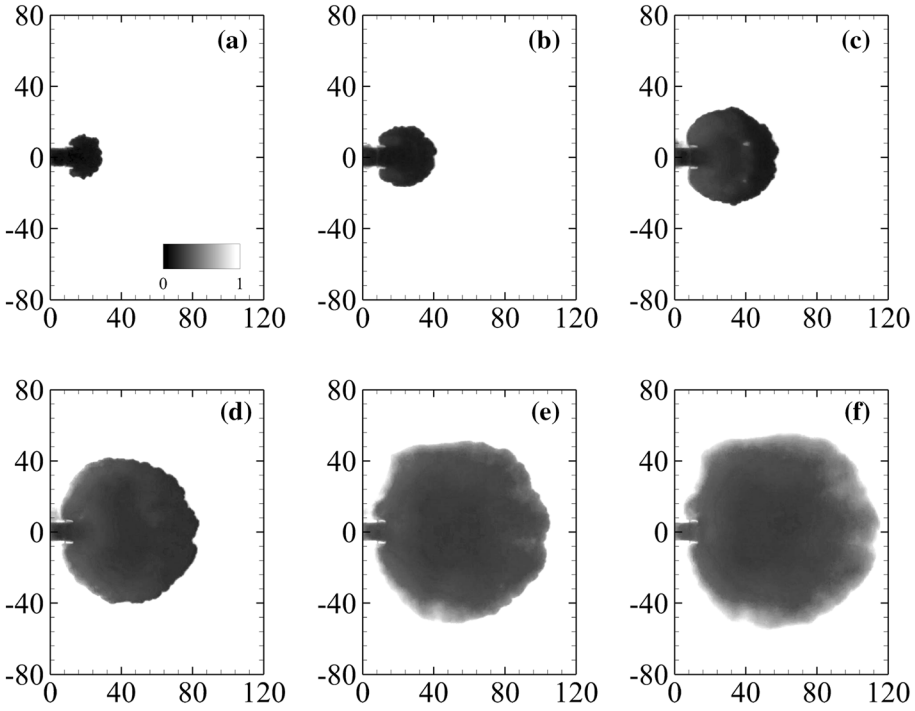

Fig. 15 Experiment 01/17/17-4: top view images for the gravity current propagating on an unbounded horizontal boundary. The reduced gravity in this experiment was $g_0' = 17.12$ cm s^{-2}. Distances in the downslope and spanwise directions are in units of cm. Time instances are chosen at **a**–**f** $t = 4, 6, 10, 20, 40, 60$ s

for the gravity currents on the 12°, 9° and 6° unbounded uniform slopes. Therefore, the power-relationship (12) applies in the late stage of the deceleration phase and the application of the power-relationship (12) suggests a balance between the buoyancy and viscous forces. The equation of the straight line of best fit to the late deceleration phase is $(x_f + x_0)^4 = K_{VM} B^{2/3} V_0^{2/3} \nu^{-1/3} (t + t_{VM})$, where $K_{VM} = 54.52$ and $t_{VM} = -17.29$ s. The experimental constant K_{VM}, as listed in Table 3, is calculated according to (12) and based on the slope of the best fit line to the late deceleration phase and other relevant parameters in (12).

Table 3 Table showing the dependent variables for the gravity currents propagating on 3°, 0° slopes, including the distance from the virtual origin to the lock gate x_0, experimental constants K_I, t-intercept t_I in (9), experimental constant K_{VM} and t-intercept t_{VM} in (12)

θ	x_0 (cm)	K_I	t_I (s)	K_{VM}	t_{VM} (s)
3°	$12.23^{+4.23}_{-7.23}$	$14.36^{+3.12}_{-2.27}$	$-0.96^{+1.85}_{-2.52}$	$63.21^{+16.91}_{-15.77}$	$-23.06^{+5.77}_{-7.93}$
0°	$6.84^{+3.15}_{-3.83}$	$6.59^{+1.63}_{-2.02}$	$0.77^{+1.48}_{-1.64}$	$7.52^{+5.03}_{-3.45}$	$20.43^{+30.67}_{-28.77}$

The subscripts I and VM represent the inertial phase and viscous phase for the gravity currents on a 3° unbounded uniform slope and on an unbounded horizontal boundary, respectively

4.4 Gravity currents on a horizontal boundary

In order to compare with the gravity currents propagating on a 3° slope and on other slopes, we also performed the experiments on the gravity currents propagating on a horizontal boundary. The top view images of the gravity current on a horizontal boundary are shown in Fig. 15. Overall, the flow morphology is qualitatively similar to the gravity current on a 3° slope but different from the gravity currents on the 12°, 9° and 6° unbounded uniform slopes. After released from the lock, the heavy fluid spreads outward continuously throughout the motion. The gravity current on a horizontal boundary maintains an integrated shape which is more akin to a circular disk expanding on the plane rather than a wedge shape as the gravity currents propagating on the 12°, 9° and 6° unbounded uniform slopes. We should note that a shape similar to a circular disk was also observed for the unconfined gravity currents on a horizontal boundary in the studies of [19, 26].

Figure 16 shows the front velocity history for the gravity current propagating on a horizontal boundary. As can be expected based on the knowledge of the propagation of cylindrical gravity currents on a horizontal boundary [5, 14], one acceleration phase is observed in this case. After reaching the maximum front velocity, the gravity current moves into the deceleration phase. In the early stage of the deceleration phase when the buoyancy and inertia forces are in balance, the power-relationship (9) applies for the gravity current propagating on a horizontal boundary as do the gravity currents on other slopes in our study. In the late stage of the deceleration phase, as the gravity current on a horizontal boundary maintains a circular disk shape, the power-relationship (12) applies when the buoyancy and viscous forces are in balance.

Figure 17a shows $(x_f + x_0)^2$ versus t and the fitting equation for the straight line of best fit in the early deceleration phase is $(x_f + x_0)^2 = \left(K_I B\right)^{1/2}(t + t_I)$, where $K_I = 7.57$, $B = 13696$ cm^4 s^{-2}, $x_0 = 5.23$ cm and $t_I = 0.13$ s. Our reported values of K_I for the gravity current on a horizontal boundary, as listed in Table 3, are consistent with but slightly greater than the estimates of 5.71 and 3.62 based on the experiments of [17, 18]. Such a slight difference may be attributed to the fact that, while the gravity currents spread radially outward in [17, 18], the gravity currents produced in our lock configuration propagate preferentially in the direction towards the gate when the gate is removed. The front

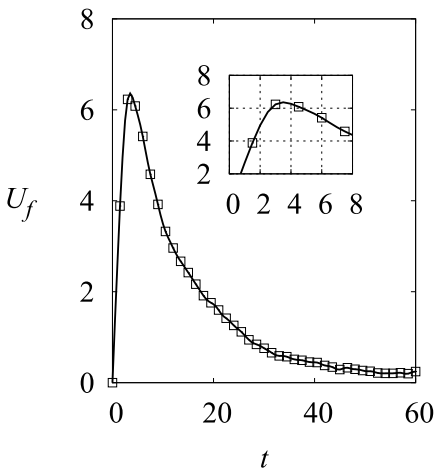

Fig. 16 Experiment 01/17/17-4: front velocity history for the gravity current propagating on an unbounded horizontal boundary. The reduced gravity in this experiment was $g_0' = 17.12$ cm s^{-2}. The maximum front velocity $U_{f_{max}} \approx 6.36$ cm s^{-1} occurs at $t \approx 3.50$ s. The front velocity is in units of cm s^{-1} and time is in units of s

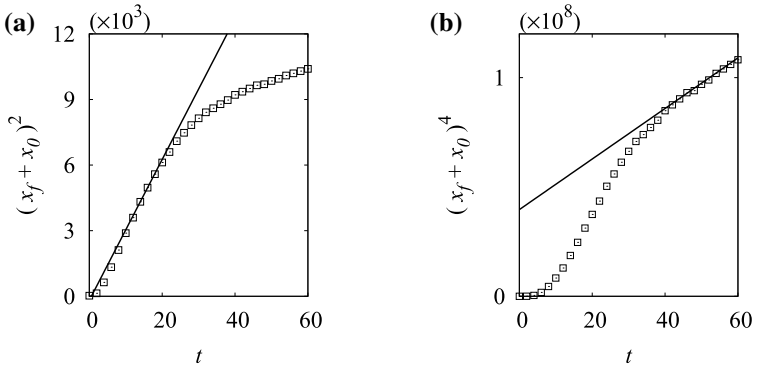

Fig. 17 Experiment 01/17/17-4: relationship between **a** $(x_f + x_0)^2$ and t and **b** $(x_f + x_0)^4$ and t for the gravity current propagating on an unbounded horizontal boundary. The reduced gravity in this experiment was $g_0' = 17.12$ cm s $^{-2}$. The front location is in units of cm and time is in units of s. The solid line in **a** represents the straight line of best fit to the early deceleration phase and the fitting equation is $(x_f + x_0)^2 = \left(K_I B\right)^{1/2}(t + t_I)$, where $K_I = 7.57$, $B = 13696$ cm^4 s^{-2}, $x_0 = 5.23$ cm and $t_I = 0.13$ s. The solid line in **b** represents the straight line of best fit to the late decelearation phase and the fitting equation is $(x_f + x_0)^4 = K_{VM} B^{2/3} V_0^{2/3} \nu^{-1/3}(t + t_{VM})$, where $K_{VM} = 4.17$ and $t_{VM} = 51.10$ s. The maximum front velocity $U_{f\,max} \approx 6.36$ cm s^{-1} occurs at $t \approx 3.50$ s

location history robustly follows the power-relationship (9) during $10 \lesssim t \lesssim 20$ s. Afterwards, the front location history begins to deviate from the power-relationship (9) when the front Reynolds number is about $\mathrm{Re}_f \approx 500$. Figure 17b shows $(x_f + x_0)^4$ versus t and the fitting equation for the straight line of best fit in the late deceleration phase is $(x_f + x_0)^4 = K_{VM} B^{2/3} V_0^{2/3} \nu^{-1/3}(t + t_{VM})$, where $K_{VM} = 4.17$ and $t_{VM} = 51.10$ s. Again, our reported values of K_{VM} for the gravity current on a horizontal boundary, as listed in Table 3, are consistent with but slightly greater than the estimate based on [17].

In summary, we reported the gravity currents propagating on 12°, 9°, 6°, 3° unbounded uniform slopes and on an unbounded horizontal boundary. After the initial acceleration phase, the gravity currents move into the early and late stage of the deceleration phase. In the early stage of the deceleration phase, the front location history follows the power-relationship (9). In the late stage of the deceleration phase for the gravity currents on 12°, 9°, 6° unbounded uniform slopes, the front location history follows (11) while in the late stage of the deceleration phase for the gravity currents on a 3° unbounded uniform slope and on an unbounded horizontal boundary, the front location history follows (12). We should remark that the gravity currents on 12°, 9°, 6° unbounded uniform slopes maintain a wedge shape in the early deceleration phase an 'active' head separates from the body of the current in the late deceleration phase. The gravity currents on a 3° unbounded uniform slope and on an unbounded horizontal boundary maintain an integrated shape throughout the propagation.

5 Conclusions

Gravity currents produced from a finite volume of heavy fluid propagating on 12°, 9°, 6°, 3° unbounded uniform slopes and on an unbounded horizontal boundary are presented. The novel contribution of this work is that, while the heavy fluid is released from the lock with a quiescent condition, there are two stages of the deceleration phase for the

gravity currents on unbounded uniform slopes. The flow morphologies in the early stage and late stage of the deceleration phase for the gravity currents propagating on 12°, 9° and 6° unbounded uniform slopes are qualitatively different from those for the gravity currents propagating on a 3° unbounded uniform slope and on an unbounded horizontal boundary.

For the gravity currents propagating on 12°, 9°, 6° unbounded uniform slopes in the early stage of the deceleration phase, the buoyancy force and the inertia force are in balance and the front location history follows the power-relationship (9). The experimental constant K_I monotonically increases with the slope angle from $K_I = 57.52^{+4.23}_{-8.03}$ at $\theta = 6°$ to $K_I = 79.78^{+2.41}_{-3.93}$ at $\theta = 9°$ and $K_I = 92.99^{+5.75}_{-5.02}$ at $\theta = 12°$. Furthermore, the front location history begins to deviate from the power-relationship in the early deceleration phase when the front Reynolds number falls to $\mathrm{Re}_f \approx 2000 \sim 3000$ and the viscous force becomes more important. In the late stage of the deceleration phase, an 'active' head separates from the body of the current and the front location history follows the power-relationship (11). The experimental constant K_{VS} increases with the slope angle from $K_{VS} = 2.99^{+2.22}_{-2.26}$ at $\theta = 6°$ to $K_{VS} = 4.09^{+0.08}_{-0.07}$ at $\theta = 9°$ and $K_{VS} = 4.43^{+0.78}_{-1.01}$ at $\theta = 12°$. As a general belief in the study of gravity currents [46], the viscous effects are thought to be negligible compared with inertial effects in the propagation of gravity currents for the Reynolds number greater than 1000, but the gravity currents propagating on 12°, 9° and 6° unbounded uniform slopes might be an exception to this general belief.

For the gravity currents propagating on a 3° unbounded uniform slope and on an unbounded horizontal boundary in the early stage of the deceleration phase, the front location history also follows the power-relationship (9). The experimental constant K_I increases with the slope angle from $K_I = 6.59^{+1.63}_{-2.02}$ at $\theta = 0°$ to $K_I = 14.36^{+3.12}_{-2.27}$ at $\theta = 3°$. The front location history begins to deviate from the power-relationship in the early deceleration phase when the front Reynolds number falls to $\mathrm{Re}_f \approx 500 \sim 1000$ and the gravity currents move into the late stage of the deceleration phase. In the late stage of the deceleration phase, the gravity currents on a 3° unbounded uniform slope and on an unbounded horizontal boundary maintain an integrated circular disk shape without violent mixing with the ambient fluid and the front location history follows the power-relationship (12). The experimental constant K_{VM} increases with the slope angle from $K_{VM} = 7.52^{+5.03}_{-3.45}$ at $\theta = 0°$ to $K_{VM} = 63.21^{+16.91}_{-15.77}$ at $\theta = 3°$. Our reported values of K_I and K_{VM} for the gravity currents on a horizontal boundary are also in reasonable agreement with the estimates based on previously published experiments [17, 18].

Our experiments show that the gravity currents on 12°, 9°, 6° unbounded uniform slopes in the late stage of the deceleration phase have an 'active' head which separates from the body of the current and the gravity currents on a 3° unbounded uniform slope and on an unbounded horizontal boundary in the late stage of the deceleration phase maintain an integrated shape. Our results indicate two possible routes to the final stage of the gravity currents on unbounded uniform slopes.

Acknowledgements A. D. is grateful for encouragement from Professors P. Linden and S. Dalziel at the University of Cambridge, S. Balachandar at the University of Florida, M. Garcia and G. Parker at the University of Illinois at Urbana-Champaign. Funding supports from National Taiwan University through Grant 109L7830 and from Taiwan Ministry of Science and Technology through Grant MOST-105-2221-E-002-125-MY2 are greatly acknowledged.

Compliance with ethical standards

Conflict of interest The authors declare that they have no conflict of interest.

References

1. Adduce C, Sciortino G, Proietti S (2012) Gravity currents produced by lock-exchanges: experiments and simulations with a two layer shallow-water model with entrainment. J Hydraul Eng 138(2):111–121
2. Batchelor GK (1967) An introduction to fluid dynamics. Cambridge University Press, Cambridge
3. Beghin P, Hopfinger EJ, Britter RE (1981) Gravitational convection from instantaneous sources on inclined boundaries. J Fluid Mech 107:407–422
4. Bonnecaze RT, Lister JR (1999) Particle-driven gravity currents down planar slopes. J Fluid Mech 390:75–91
5. Cantero M, Balachandar S, Garcia M (2007) High-resolution simulations of cylindrical density currents. J Fluid Mech 590:437–469
6. Dade WB, Lister JR, Huppert HE (1994) Fine-sediment deposition from gravity surges on uniform slopes. J Sed Res 64:423–432
7. Dai A (2010) Note on the generalized thermal theory for gravity currents in the deceleration phase. Dyn Atmos Oceans 50:424–431
8. Dai A (2013) Experiments on gravity currents propagating on different bottom slopes. J Fluid Mech 731:117–141
9. Dai A (2013) Power-law for gravity currents on slopes in the deceleration phase. Dyn Atmos Oceans 63:94–102
10. Dai A (2014) Non-Boussinesq gravity currents propagating on different bottom slopes. J Fluid Mech 741:658–680
11. Dai A (2015) High-resolution simulations of downslope gravity currents in the acceleration phase. Phys Fluids 27:076602
12. Dai A, Huang YL (2016) High-resolution simulations of non-Boussinesq downslope gravity currents in the acceleration phase. Phys Fluids 28:026602
13. Dai A, Ozdemir CE, Cantero MI, Balachandar S (2012) Gravity currents from instantaneous sources down a slope. J Hydraul Eng 138(3):237–246
14. Dai A, Wu CS (2016) High-resolution simulations of cylindrical gravity currents in a rotating system. J Fluid Mech 806:71–101
15. Ellison TH, Turner JS (1959) Turbulent entrainment in stratified flows. J Fluid Mech 6:423–448
16. Hopfinger EJ (1983) Snow avalanche motion and related phenomena. Annu Rev Fluid Mech 15:47–76
17. Hoult DP (1972) Oil spreading on the sea. Annu Rev Fluid Mech 4:341–368
18. Huppert HE, Simpson JE (1980) The slumping of gravity currents. J Fluid Mech 99:785–799
19. Inghilesi R, Adduce C, Lombardi V, Roman F, Armenio V (2018) Axisymmetric three-dimensional gravity currents generated by lock exchange. J Fluid Mech 851:507–544
20. Jones CS, Cenedese C, Chassignet EP, Linden PF, Sutherland BR (2014) Gravity current propagation up a valley. J Fluid Mech 762:417–434
21. Korotkin AI (2008) Added masses of ship structures, 1st edn. Springer, Berlin
22. Kyrousi F, Leonardi A, Roman F, Armenio V, Zanello F, Zordan J, Juez C, Falcomer L (2018) Large Eddy simulations of sediment entrainment induced by a lock-exchange gravity current. Adv Water Resour 114:102–118
23. La Rocca M, Adduce C, Lombardi V, Sciortino G, Hinkermann R (2012) Developement of a lattice Boltzmann method for two-layered shallow-water flow. Int J Numer Methods Fluids 70(8):1048–1072
24. La Rocca M, Adduce C, Sciortino G, Bateman PA, Boniforti MA (2012) A two-layer shallow water model for 3D gravity currents. J Hydraul Res 50(2):208–217
25. La Rocca M, Adduce C, Sciortino G, Pinzon AB (2008) Experimental and numerical simulation of three-dimensional gravity currents on smooth and rough bottom. Phys Fluids 20(10):106603
26. Lombardi V, Adduce C, La Rocca M (2018) Unconfined lock-exchange gravity currents with variable lock width: laboratory experiments and shallow-water simulations. J Hydraul Res 56(3):399–411
27. Lombardi V, Adduce C, Sciortino G, La Rocca M (2015) Gravity currents flowing upslope: laboratory experiments and shallow-water simulations. Phys Fluids 27:016602
28. Marleau LJ, Flynn MR, Sutherland BR (2014) Gravity currents propagating up a slope. Phys Fluids 26:046605
29. Martin A, Negretti ME, Ungarish M, Zemach T (2020) Propagation of a continuously supplied gravity current head down bottom slopes. Phys Rev Fluid 5(5):054801
30. Maxworthy T (2010) Experiments on gravity currents propagating down slopes. Part 2: The evolution of a fixed volume of fluid released from closed locks into a long, open channel. J Fluid Mech 647:27–51

31. Maxworthy T, Nokes RI (2007) Experiments on gravity currents propagating down slopes. J Fluid Mech 584:433–453
32. Morton BR, Taylor GI, Turner JS (1956) Turbulent gravitational convection from maintained and instantaneous sources. Proc R Soc A 234:1–23
33. Negretti ME, Flòr JB, Hopfinger EJ (2017) Development of gravity currents on rapidly changing slopes. J Fluid Mech 833:70–97
34. Ottolenghi L, Adduce C, Inghilesi R, Armenio V, Roman F (2016) Entrainment and mixing in unsteady gravity currents. J Hydraul Res 54(5):541–557
35. Ottolenghi L, Adduce C, Inghilesi R, Roman F, Armenio V (2016) Mixing in lock-release gravity currents propagating up a slope. Phys Fluids 28:056604
36. Ottolenghi L, Adduce C, Roman F, Armenio V (2017) Analysis of the flow in gravity currents propagating up a slope. Ocean Model 115:1–13
37. Ottolenghi L, Cenedese C, Adduce C (2017) Entrainment in a dense current flowing down a rough sloping bottom in a rotating fluid. J Phys Oceanogr 47(3):485–498
38. Ottolenghi L, Prestininzi P, Montessori A, Adduce C, La Rocca M (2018) Lattice Boltzmann simulations of gravity currents. Eur J Mech B/Fluids 67:125–136
39. Ouillon R, Meiburg E, Sutherland BR (2019) Turbidity currents propagating down a slope into a stratified saline ambient fluid. Environ Fluid Mech 19(5):1143–1166
40. Pawlak G, Armi L (2000) Mixing and entrainment in developing stratified currents. J Fluid Mech 424:45–73
41. Pérez-Díaz B, Castanedo S, Palomar P, Henno F, Wood M (2019) Modeling nonconfined density currents using 3D hydrodynamic models. J Hydraul Eng 145(3):04018088
42. Pérez-Díaz B, Palomar P, Castanedo S, Álvarez A (2018) PIV-PLIF characterization of nonconfined saline density currents under different flow conditions. J Hydraul Eng 144(9):04018063
43. Rastello M, Hopfinger EJ (2004) Sediment-entraining suspension clouds: a model of powder-snow avalanches. J Fluid Mech 509:181–206
44. Ross AN, Linden PF, Dalziel SB (2002) A study of three-dimensional gravity currents on a uniform slope. J Fluid Mech 453:239–261
45. Shin J, Dalziel S, Linden PF (2004) Gravity currents produced by lock exchange. J Fluid Mech 521:1–34
46. Simpson JE (1997) Gravity currents, 2nd edn. Cambridge University Press, Cambridge
47. Steenhauer K, Tokyay T, Constantinescu G (2017) Dynamics and structure of planar gravity currents propagating down an inclined surface. Phys Fluids 29(3):036604
48. Tickle G (1996) A model of the motion and dilution of a heavy gas cloud released on a uniform slope in calm conditions. J Hazard Mater 49:29–47
49. Ungarish M (2009) An introduction to gravity currents and intrusions. Chapman & Hall/CRC Press, Routledge
50. Webber D, Jones S, Martin D (1993) A model of the motion of a heavy gas cloud released on a uniform slope. J Hazard Mater 33:101–122
51. Whitehead JA, Chapman DC (1986) Laboratory observations of a gravity current on a sloping bottom: the generation of shelf waves. J Fluid Mech 172:373–399
52. Zgheib N, Ooi A, Balachandar S (2016) Front dynamics and entrainment of finite circular gravity currents on an unbounded uniform slope. J Fluid Mech 801:322–352